JOURNAL OF SPACECRAFT AND ROCKETS
Vol. 44, No. 1, January–February 2007

Shape Memory Alloy Deployment of Membrane Mirrors for Spaceborne Telescopes

Eric L. Pollard* and Christopher H. M. Jenkins†
South Dakota School of Mines & Technology, Rapid City, South Dakota 57701-3995

DOI: 10.2514/1.17158

The objectives of this research were to develop and refine a shape memory alloy modeling approach, the martensite twin reorientation subroutine, to predict the transient response of a spaceborne membrane optic shape memory alloy deployment actuator spine system. In concert with a commercial finite element solver, this application supports multidimensional, temperature-displacement transient predictions of the shape memory effect exhibited by shape memory alloys through implementation of a phenomenological constitutive law. This article presents an original notion to numerically describe multiaxial, inelastic response of a continuum with a standard of practical utility not previously considered in the literature. The scope of this study was to model the relation of input power magnitude and waveform to stress fields, reaction forces, and thermal fields for the figure acquisition of a gossamer reflector. Of particular interest is the stress and thermal field history of the polymeric membrane concentrator through the deployment to prevent mechanical and thermal failure as limited experimental or modeling analysis results exist for shape memory alloy deployment schemes. Thermal authority over the concentrator was found locally limited to the spine interface. Upon aperture engagement, the integrated model's first excursion cycle frequency excited by all three loading regimes was nonunique, regardless of the preceding temporal character of the spine's response. This tendency suggests a coupling between the structural dynamic designs for deployment and in-service, deployed architectures. Aspects of the deployment sequence warranting further study and issues to tackle to further develop the martensite twin reorientation subroutine are identified. Technology addressed through this thesis research is intended to foster and mature successive large, launch-packaged space vehicle programs.

Nomenclature

A_f = B2 phase finish temperature
A_s = B2 phase start temperature
C_C = concentrator specific heat
C_S = spine specific heat
$\boldsymbol{D}$ = elastic modulus
E_A = B2 phase modulus of elasticity
E_C = concentrator modulus of elasticity
$E_{i,j}$ = modulus of elasticity based upon element number i and loop number j
E_M = R phase modulus of elasticity
E_S = spine modulus of elasticity
F = force
f_∞ = focal length to diameter ratio
$f_{\infty,C}$ = concentrator focal length to diameter ratio
$f_{\infty,S}$ = spine focal length to diameter ratio
$\boldsymbol{G}_{i,A}$ = nodal B2 phase geometry vector based upon node number i
$\boldsymbol{G}_{i,j}$ = nodal geometry vector based upon node number i and loop number j
$\boldsymbol{G}_{i,M}$ = nodal R phase geometry vector based upon node number i
h_C = concentrator thickness
h_S = spine thickness
K_A = B2 phase thermal conductivity
K_C = concentrator thermal conductivity
$K_{i,j}$ = thermal conductivity based upon element number i and loop number j
K_M = R phase thermal conductivity
K_S = spine thermal conductivity
N_e = number of elements
N_l = number of loops
N_n = number of nodes
P = pressure
Q_{bf} = thermal body flux
Q_c = thermal convection
q_{bf} = specific thermal body flux
R_C = concentrator radius of projected area
R_S = spine radius of projected area
r = projected area radial position
S_y = B2 phase yield stress
$T_{i,j}$ = temperature based upon element number i and loop number j
$T_{0,i}$ = initial temperature based upon element number i
t = time
$\boldsymbol{U}_{i,j}$ = nodal B2 phase global stable minima geometry displacement vector based upon node number i and loop number j
$\boldsymbol{u}_{i,j}$ = nodal displacement vector based upon node number i and loop number j
w_C = concentrator width
α_A = B2 phase coefficient of thermal expansion
α_C = concentrator coefficient of thermal expansion
$\alpha_{i,j}$ = coefficient of thermal expansion based upon element number i and loop number j
α_M = R phase coefficient of thermal expansion
α_S = spine coefficient of thermal expansion
β = SIM angle
$\boldsymbol{\varepsilon}$ = strain tensor
$\boldsymbol{\varepsilon}_0$ = initial strain tensor
$\boldsymbol{\Theta}$ = thermoelastic stress tensor
ν_C = concentrator Poisson's ratio
ν_S = spine Poisson's ratio
$\xi_{i,j}$ = martensite phase fraction internal state variable based upon element number i and loop number j

Presented as Paper 2196 at the 46th AIAA/ASME/ASCE/AHS/ASC Structures, Structural Dynamics, and Materials Conference, Austin, TX, 18–21 April 2005; received 14 April 2005; revision received 28 August 2006; accepted for publication 29 August 2006.

*Research Assistant, Compliant Structures Laboratory, 501 East St. Joseph Street. AIAA Student Member.
†Professor, Department of Mechanical Engineering, 501 East St. Joseph Street. AIAA Associate Fellow.

$\xi_{0,i}$ = initial martensite phase fraction based upon element number i
ρ_C = concentrator mass density
ρ_S = spine mass density
$\boldsymbol{\sigma}$ = stress tensor
$\sigma_{\mathrm{vm},i,j}$ = distortion energy stress based upon element number i and loop number j
$\boldsymbol{\sigma}_0$ = initial stress tensor
$\boldsymbol{\Omega}$ = detwinned stress tensor
ω_1 = first natural frequency

I. Introduction

SINCE discovery, the shape memory effect (SME) or martensite twin reorientation (MTR) has been identified as a potential agency to drive active material systems. Shape memory alloys (SMAs) are particularly attractive for space applications due to their ability to recover large deformations by generating high specific force, with reasonable energy consumption and intrinsic precision movement, an artifact of the atomistic nature of the austenite–martensite crystalline phase transformation. Although considerable advancements have been made in the evolution of tunable, reconfigurable, and actuation material systems, the crux for progress of this technology is our ability to model the thermomechanics of the SME [1]. This paper presents an original notion to numerically describe multiaxial, inelastic response of a continuum with a standard of practical utility not previously considered in the literature.

SMA components first established flight heritage on space vehicles as alternatives to pyrotechnic devices. Applications include the backup boom release onboard the ISEE-B spacecraft (1977), a solar array bearing a pin off-load and unlatching mechanism for the Hubble Space Telescope solar panels (1990), and a solar panel release onboard the Clementine spacecraft (1994) [2]. Just as these vehicles incorporated the SME, deployment and in-service challenges of gossamer spacecraft will further showcase the leverage SMA technology extends to structural reconfiguration and tuning.

Gossamer technology is anticipated to enable a paradigm revision in the approach to space system design philosophy through revolutionary spacecraft component technologies and driven by mission requirements demanding order of magnitude increases in aperture size for higher spatial and temporal resolution. Challenges of this emerging revision are deployment techniques, membrane and rigidizable materials, surface accuracy for precision reflectors, and analytical tool development. Pioneering gossamer spacecraft include the Echo balloon series (1950s and 1960s), Goodyear antennas (1960s), Contraves antennas and sunshades (1970s and 1980s), L'Garde inflatable decoys (1970s and 1980s), and L'Garde Inflatable Antenna Experiment (1996) [3]. Technology addressed through this thesis research is intended to foster and mature successive large, launch-packaged space vehicle programs.

The earliest documentation of the SME is attributed to Chang and Read [4] in 1951. Buehler and Wiley [5], in 1962, observed this phenomenon in a popular SMA while conducting materials studies at the Naval Ordinance Laboratory. This particular equiatomic nickel–titanium alloy was identified as Nitinol to incorporate the namesake of both the elemental composition and laboratory of discovery. Since Buehler and Wiley's [5] find, considerable research effort has been invested to understand the microstructural characteristics involved and to mathematically describe the response of Nitinol, as well as other metallic alloys found to exhibit similar behavior, such as the Cu–Al–Ni and Cu–Zn–Al–Mn systems. The considerable attendant recoverable inelastic strains (8–9%) and stresses (500–900 MPa for Nitinol) of the SME have perennially sustained interest in this materials technology among the aerospace community [6,7].

Several constitutive models have been proposed to mathematically describe the macroscopic mechanical behavior of SMAs. Most notably among those considered a phenomenological approach include constitutive laws developed by Tanaka and Nagaki [8], Liang and Rogers [9], Ivshin and Pence [10], Brinson [11], Boyd and Lagoudas [12], and Abeyaratne et al. [13]. These constitutive laws generally incorporate both a kinetic law governing the phase transformation and a mechanical law governing stress-strain behavior. Often the kinetic laws distil to a single state variable, the martensite fraction, as a function of temperature and stress. Models employing these laws yield relatively accurate uniaxial solutions, as they are founded on ad hoc descriptions sought to agree with empirical results. The most significant discrepancy between these models is the imbedded kinetic law as the detwinned strain often dominates the conventional elastic deformation mechanism [14].

Models based on a micromechanics approach, founded on thermodynamic principles, include those developed by Sun and Hwang [15], Patoor et al. [16], Goo and Lexcellent [17], Huang and Brinson [18], Vivet and Lexcellent [19], and Lu and Weng [20]. These micromechanical formulated constitutive laws also yield relatively accurate uniaxial solutions, but are more computationally demanding due to increased complexity. A mesomechanical model has also been proposed by Vokoun and Kafka [21] based on the general concept deformation of two-phase materials that can be represented by the opposing residual stresses of two continuous substructures.

Amenability of the three approaches to multiaxial phenomena remains a subject of investigation. Promise in overcoming the complications of mathematically describing multidimensional SME has been demonstrated by Liang and Rogers [22], Boyd and Lagoudas [12], a hybrid microplane approach proposed by Brocca et al. [23], and multidimensional finite variant extension from the one-dimensional Liang and Rogers model developed by Pollard [24].

The objectives of this research were to develop and refine an SMA modeling approach, the MTR subroutine, to predict the transient response of a spaceborne membrane optic SMA deployment actuator spine system (Fig. 1). Motivation for this figure acquisition concept can be sought by studying thermonasty, or plant movement response to temperature. Tensioning a compliant concentrator with thermally activated spines falls under the same rubric as the blooming of a flower.

One-time actuation of said monolithic actuator is anticipated achievable by tailoring a SMA through the variation of elemental fractions and introduction of impurities. The scope of this study was to model the relation of input power magnitude and waveform to stress fields, reaction forces, and thermal fields for the figure acquisition of a gossamer reflector. Of particular interest is the stress and thermal field history of the polymeric membrane concentrator through the deployment to prevent mechanical and thermal failure as limited experimental or modeling analysis results exist for SMA deployment schemes. Establishing accurate and practical methods for modeling the deployment dynamics of gossamer structures, specifically to forecast spacecraft loads, permits examination of different material choices, and packaging strategies are considered key to expedite the end use of this enabling technology [3].

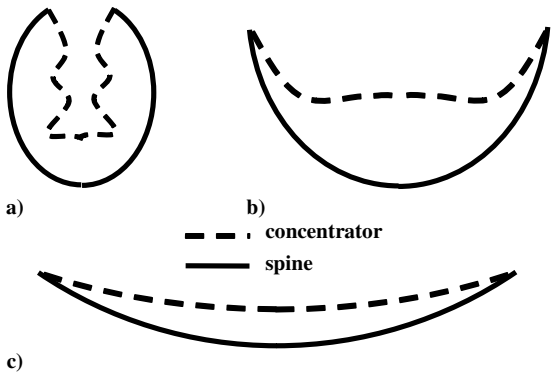

Fig. 1 Spaceborne membrane optic SMA actuator spine system deployment sequence concept, a) stowed configuration; b) partially deployed; c) deployed architecture.

II. MTR Subroutine

The developed MTR subroutine implements a phenomenological constitutive law to model the SME exhibited by SMAs. The application was initially designed to interface with the ABAQUS Explicit solver. This finite element tool supports a dynamic, fully coupled thermal-stress analysis and includes inertia effects. The transient thermal response is modeled by employing continuum elements [25]. Predictions of the shape memory effect require the temperature and displacement degrees of freedom (DOFs) to be solved simultaneously.

Acceleration solutions are calculated at each time step to satisfy dynamic equilibrium from the equations of motion. The kinematic state is advanced by employing a conditionally stable, central difference explicit integration rule and structuring the mass matrices diagonally for computational efficiency. Element by element automatic time incrementation ensures the integration time step is approximately equivalent to the least elemental dilation wave transient time speed. The Explicit package also considers nonlinear geometry, computes in double machine precision, and supports Rayleigh structural and fluid damping [25].

A. Theory

Calculation of the martensite phase fraction internal state variable ξ is based on an empirical model developed by Liang and Rogers [9]. This model accounts for the chemical free energy of temperature and stress, fitting the phase transformation kinetics to a cosine function based on the austenite start and finish temperatures, A_s and A_f, and the current temperature of the alloy T; the shape of the hysteresis envelope resembles a sinusoid. The form of this model implemented in the MTR subroutine accounts for stress induced martensite (SIM) through the term driven by the distortion energy stress σ_{vm}, nondimensionalized by the yield stress S_y, at a rate inversely proportional to the tangent of β, inherently discounting superelasticity occurring above the austenite finish temperature [Eq. (1)]. The maximum martensite phase fraction value of unity corresponds to complete rhombohedral (R) phase transformation.

$$\xi_{i,j+1}(T_{i,j},\sigma_{\text{vm},i,j}) = \frac{\xi_{0,i}}{2}\left[1+\cos\left(\frac{\pi}{(A_f-A_s)}(T_{i,j}-A_s) - \frac{\pi}{(A_f-A_s)}\frac{A_f}{\tan\beta}\frac{|\sigma_{\text{vm},i,j}|}{S_y}\right)\right] \tag{1}$$

where

$$\frac{\tan\beta}{A_f}[(T_{i,j}-A_s)-(A_f-A_s)] \le \frac{|\sigma_{\text{vm},i,j}|}{S_y} \le \frac{\tan\beta}{A_f}(T_{i,j}-A_s)$$

$$i = 1,2,\ldots,N_e$$

$$j = 1,2,\ldots,N_l$$

The theory founding the MTR subroutine hypothesizes any global geometry not exceeding the maximum recoverable strain limit is a potential stable minimum energy state once the alloy has assumed R atomic ordering. Conventional plastic deformation is not supported. As the SMA is subjected to stress to achieve an altered configuration or deformed R phase geometry, the lattice responds by reorienting the crystalline structure through detwinning and a new global geometry stable minimum is sought corresponding to the altered state of the crystal lattice for a given temperature and stress. For a one-way phase transformation from the R phase to the body-centered cubic (B2) phase, the initial configuration of the finite element nodes modeling the SMA is consistent with the deformed R phase geometry stable minimum. A two-phase crystalline structure, both R and B2, is transient and global geometries through the R phase to B2 phase transformation are considered unstable.

It is possible to relate the implementation of the MTR subroutine model to the unified constitutive relation published by Liang and Rogers [9] among others, where the stress $\boldsymbol{\sigma}-\boldsymbol{\sigma}_0$ depends on the elastic stress term $\boldsymbol{D}(\boldsymbol{\varepsilon}-\boldsymbol{\varepsilon}_0,\xi)$, referencing the current stable or unstable minimum geometry, the inelastic stress term $\boldsymbol{\Omega}(\xi-\xi_0)$, accounting for the discrepancy from the trained shape or B2 stable minimum geometry to the current stable or unstable minimum geometry, and the thermoelastic stress term $\boldsymbol{\Theta}(T-T_0,\xi)$, referencing the current stable or unstable minimum geometry [Eq. (2)].

$$\boldsymbol{\sigma}-\boldsymbol{\sigma}_0 = \boldsymbol{D}(\varepsilon-\varepsilon_0,\xi)+\boldsymbol{\Omega}(\xi-\xi_0)+\boldsymbol{\Theta}(T-T_0,\xi) \tag{2}$$

The tensors can represent one-, two-, or three-dimensional stress fields. If the continuum is initialized at a mechanically and thermally unloaded equilibrium, R phase configuration for a B2 phase stable minimum geometry recovery analysis, both second order tensor naught values would be zero, $\xi_0 = 1$, and T_0 would be less than A_s. The elastic modulus as a function of the martensite phase fraction internal state variable is defined as $\boldsymbol{D}(\boldsymbol{\varepsilon}-\boldsymbol{\varepsilon}_0,\xi)$. This term is modeled continuously through the ABAQUS linear elastic material law.

The detwinned stress, also a function of the martensite phase fraction internal state variable, is defined as $\boldsymbol{\Omega}(\xi-\xi_0)$ and is modeled discreetly by updating the nodal geometry vectors between successive loop analyses. As the model retransforms back to the B2 phase, the nodal geometry vectors mapping neighboring nodes track from the configuration consistent with the R phase global stable minimum,

$$\boldsymbol{G}_{i+1,M}-\boldsymbol{G}_{i,M}$$

where

$$i = 1,2,\ldots,N_n-1$$

to the configuration consistent with the B2 phase global stable minimum,

$$\boldsymbol{G}_{i+1,A}-\boldsymbol{G}_{i,A}$$

where

$$i = 1,2,\ldots,N_n-1$$

forming a set of unstable minimum energy states through the transformation along paths coincident with both R and B2 phase geometries. Mimicking MTR by defining these transformation vectors is requisite for a high fidelity model as there is only one atomistic path from lower to higher symmetry between the R and B2 phase crystalline structures. This term $\boldsymbol{\Omega}(\xi-\xi_0)$, in effect, realizes and imposes increased detwinned strain as the martensite phase fraction internal state variable decreases,

$$\boldsymbol{G}_{i+1,j+1}(\boldsymbol{G}_{i,j},\xi_{i+1,j}) = \boldsymbol{G}_{i,j}+\xi_{i+1,j}(\boldsymbol{G}_{i+1,M}-\boldsymbol{G}_{i,M}) + (1-\xi_{i+1,j})(\boldsymbol{G}_{i+1,A}-\boldsymbol{G}_{i,A}) \tag{3}$$

where

$$i = 1,2,\ldots,N_n-1$$

and

$$j = 1,2,\ldots,N_l$$

and consequently drives the return to the parent configuration with no associated detwinned stress, that is, the trained austenite shape.

This constituent hypothesis is the crux of the subroutine's approach to emulate the SME. Mapping originates from nodes of known configuration; reviewing Eq. (3), node $i = 1$ would be declared at an essential boundary. Progress along the transformation paths is proportional to the martensite phase fraction internal state variable. This set of unstable minima is not strictly globally

deterministic because the paths the nodal geometry vectors track are relative to the configuration of neighboring nodes, but these vectors do have a strong attraction to the B2 phase global stable minimum geometry. Elemental discretization of the martensite phase fraction supports unique transformation paths and consequently discretization of the SME to the finite element scale. The relative nature of the nodal geometry vectors does not compromise global deployment destiny because only one parent phase global stable minimum configuration is possible.

The MTR subroutine capability is limited to one-way phase transformations from martensite to austenite; two-way and superelasticity behavior is not supported. As the subroutine was designed to be implemented in conjunction with a deployment model not to exceed the threshold stress, these phenomena were not of concern. Consistent with the proposed theory, the subroutine reassigns nodal geometry vectors, as well as phase dependent properties, including modulus of elasticity, coefficient of thermal expansion (CTE), and thermal conductivity, proportional to the Liang and Rogers martensite phase fraction internal state variable between ABAQUS analyses [Eqs. (4–6)]. The duration of these analyses is orders of magnitude less than the period of the model's first austenitic mode to avoid influence sensitivity at the natural frequency and ensure sufficient temporal discretization.

$$E_{i,j+1}(\xi_{i,j}) = \xi_{i,j}E_M + (1 - \xi_{i,j})E_A \tag{4}$$

where

$$i = 1, 2, \ldots, N_e$$

$$j = 1, 2, \ldots, N_l$$

$$\alpha_{i,j+1}(\xi_{i,j}) = \xi_{i,j}\alpha_M + (1 - \xi_{i,j})\alpha_A \tag{5}$$

where

$$i = 1, 2, \ldots, N_e$$

$$j = 1, 2, \ldots, N_l$$

$$K_{i,j+1}(\xi_{i,j}) = \xi_{i,j}K_M + (1 - \xi_{i,j})K_A \tag{6}$$

where

$$i = 1, 2, \ldots, N_e$$

$$j = 1, 2, \ldots, N_l$$

The subroutine maintains displacements first order continuously differentiable and temperatures zeroth order continuously differentiable by imposing boundary conditions of displacement and velocity, and initial conditions of temperature, at the beginning of each analysis transcribed from the final values of the previous analysis. Boundary condition steps are required for the mechanical DOFs because the ABAQUS Explicit solver will not permit displacement discontinuities. These conditions are imposed over durations many orders of magnitude less than the period of the model's first austenitic mode to minimize their influence on the simulation.

B. Architecture

As discussed, spatial discretization of the SME is to the elemental level of the finite element model (FEM) and temporal discretization is to the interval of the ABAQUS analyses. Recall the subroutine updates the relative nodal geometry vectors discretely between ABAQUS analyses to realize and impose increased detwinned strain proportional to the martensite phase fraction internal state variable. A simulation run is composed of many ABAQUS analyses and MTR subroutine executions as illustrated in the loop map (Fig. 2).

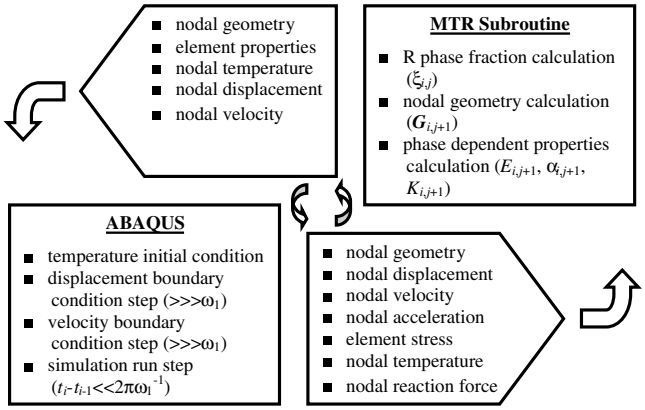

Fig. 2 ABAQUS and MTR subroutine simulation run loop architecture.

A simulation run for a given model is primed with an ABAQUS analysis of an input file enforcing the initial conditions. Typically, the SMA components of the FEM are assumed to be completely martensitic at the commencement of the run; the initial configuration of their respective finite element nodes is consistent with the deformed R phase geometry stable minimum. A unique element set and material property definition is associated with each SMA element to allow discretization of the SME to the finite element scale for the four material properties dependent upon the phase transformation. ABAQUS Explicit permits temperature initial conditions to be enforced. These DOFs, generally initialized below the B2 phase start temperature, are imposed on all the nodes of the model before the solver analyzes the steps. This component of the input file maintains temperatures zeroth order continuously differentiable between subsequent loop analyses.

The first step is composed of a displacement boundary condition with authority over all the nodes of the model. This component of the input file enforces any initial elastic strain and maintains displacements zeroth order continuously differentiable between subsequent loop analyses. The second step of the input file is composed of a velocity boundary condition with authority over all the nodes of the model. This component of the input file enforces any initial strain rate and maintains displacements first order continuously differentiable between subsequent loop analyses.

The magnitude of both these essential boundary conditions is proportional to a linear amplitude profile defined by a function coincident with zero and unity at the beginning and end of the step, respectively. To optimize for computational efficiency, the duration of the first two steps is generally set at 1 order of magnitude greater than the least elemental dilation transient time wave speed of the FEM. Modeling activity at rates greater than this FEM property is not communicated through the continuum to be included in the equilibrium calculations and results in an unstable solution. Both of these steps respect the mechanical essential boundary conditions defined for the model.

The third step is the only step of an individual ABAQUS analysis contributing to the simulation run solution. In effect, each third step solution can be considered a finite segment of the model history. In addition to also respecting the mechanical essential boundary conditions, thermal essential and mechanical and thermal natural boundary conditions, including tractions and body loads as defined for the model, are included. The duration of this step is often found between competing trends of SME temporal discretization demands and computational capacity.

Upon completion of an ABAQUS analysis, the binary results file is converted to ASCII format to be read by the MTR subroutine. The

first component of the subroutine captures the nodal configurations. Through practice it was discovered ABAQUS does not transcribe nodal geometry vectors from the input file to the results file in double precision. To maintain simulation run double precision, the nodal declarations are read directly from the input file.

The second component of the MTR subroutine captures final third step nodal displacements, velocities, accelerations, temperatures, and reaction forces and elemental distortion energy stresses from the converted ABAQUS results file. After a set interval of simulation run loops, N_l, dictated by model history resolution requirements, these solutions are appended to the simulation run solution log results file. The logged displacements are manipulated to yield identical nodal positions as displaced from the B2 phase global stable minimum geometry; this vector is defined as the mapping of the configuration resulting from inelastic strain and displacements from elastic strain,

$$\boldsymbol{G}_{i,j} + \boldsymbol{u}_{i,j}$$

from the B2 phase geometry,

$$\boldsymbol{U}_{i,j}(\boldsymbol{G}_{i,j}, \boldsymbol{u}_{i,j}) = \boldsymbol{G}_{i,j} + \boldsymbol{u}_{i,j} - \boldsymbol{G}_{i,A} \tag{7}$$

where

$$i = 1, 2, \ldots, N_n$$

and

$$j = 1, 2, \ldots, N_l$$

Both R and B2 phase nodal configurations are embedded in the subroutine. A log file, with displacement results applicable to a single model, enables continuous postprocessing of the simulation run solution as opposed to processing the ABAQUS analyses third step results individually, with the respective unique nodal declarations.

To prepare for calculating the Liang and Rogers martensite phase fraction internal state variable for each element, the subroutine distills an average elemental temperature from the temperatures of the nodes defining the element. B2 phase start and finish temperatures, B2 phase yield stress, and the SIM angle, as well as elemental initial martensite phase fraction are embedded in the subroutine. With all the R phase fraction variables accounted, Eq. (1) is solved for each element followed by Eq. (3) for each node. As discussed, the relative nodal geometry vector formulation respects the mechanical constraints defined for the model. With this approach, geometries of constrained nodes are considered constants, serving as a ground for the calculation of the unconstrained node declarations. Phase dependent properties are then solved for at the finite elemental scale based on the R and B2 phase values also embedded in the subroutine as Eqs. (4–7).

Upon executing these tasks, the next component of the MTR subroutine writes an ABAQUS input file with the three step architecture to enter into the next loop of the simulation run. Loops are completed until the model history of interest is solved.

C. Validation

With the MTR subroutine operational, experimental studies of beam test articles were conducted to validate the fidelity of the MTR subroutine and support tuning of parameters governing structural damping and the SIM phenomenon. These deflected R phase beam specimens were subjected to a series of temperature ramp magnitudes to represent various body flux or ohmic heating thermal inputs. Restraining force loads were applied at the deflected boundary to invoke responses under various expected in-service functional specifications.

1. Experimental Design

A TA Instruments Q800 dynamic mechanical analyzer (DMA) was configured with a single cantilever clamp fixture for the experimental studies to simulate a scaled membrane optic spine deployment actuator. The DMA single cantilever clamp arrangement

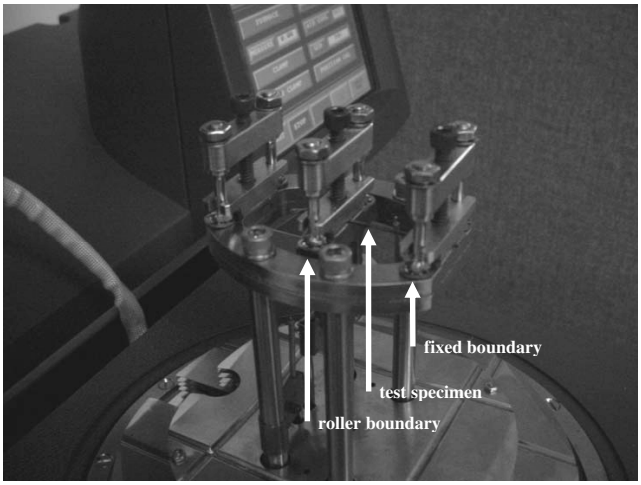

Fig. 3 DMA single or dual cantilever clamp fixture with test article mounted.

was chosen as the most representative of the envisioned figure acquisition reproduced in Fig. 1 (Fig. 3). This instrument was specified at a force resolution of 100 μN, a displacement resolution of 1.00 nm, and an isothermal stability of 100 mK [26].

The model considered to validate the fidelity of the MTR subroutine and support tuning of parameters governing structural damping and the SIM phenomenon was a fixed-roller boundary beam. This two-dimensional system allows for realizing relatively high strain potential to generated force and is applicable to many SMA actuation schemes. In addition, this setup is favorable to address life-cycle design constraints of SMA actuators, namely, the strain to fatigue degradation relation. The dimensional scale of the test specimen is a gauge length of 17.4 mm (Fig. 4).

The SMA selected for experimental work on the basis of square cross section availability was SE-508, a commercially available Nitinol alloy. A square cross section allowed for an initial coarse mesh representation of the specimen with brick elements. SE-508 strip with a 660 μm square cross section and black oxide surface finish were procured.

The specimen was subjected to a series of 16.7 and 167 mK s^{-1} linear temperature ramp magnitudes to simulate varying body flux or ohmic heating thermal loads, $Q_{\mathrm{bf}}(r, t)$. Magnitudes greater than 167 mK s^{-1} resulted in pronounced nonuniform heating of the specimen. In addition to the free recovery scenario, constant l.00 and 10.0 N restraining force loads F were applied at the roller boundary parallel to the y axis impeding the global geometry recovery to simulate return with expected in-service functional specifications, such as the inertial load of the reflector, as well as other imaging hardware.

The procedure followed for each scenario began by mounting the beam test articles in the clamps torqued to 1.10 Nm. The moveable clamp was then freed and floated to allow the specimen to assume its

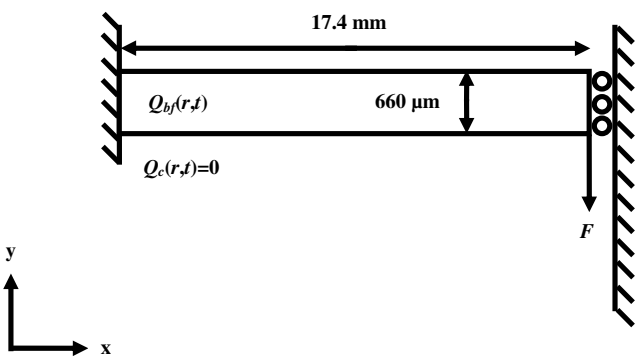

Fig. 4 Fixed-roller boundary beam actuator model.

self-weight shape. The movable clamp, previously zeroed during the calibration sequence, was locked. This step permitted the examination of gravity accelerations on the periphery displacement. Effects due to this body load were found to be approximately 116 nm and considered negligible.

The furnace was then cooled below the R phase finish temperature and maintained at this thermal condition for 180 s. After the delay, a 10.0 N load was engaged at the roller boundary in the direction of the gravity vector or the negative y-unit vector and paused for 180 s. This load was then either disengaged or adjusted to the magnitude of the restraining force and maintained for 180 s. This periphery displacement was assumed to be characteristic of the deformed R phase geometry of the beam. (The detwinned configuration for all scenarios qualified within the range of recoverable inelastic strains for Nitnol [6].)

After this third delay the linear temperature ramp load was engaged and, if applicable, the restraining force was maintained. Recorded temperature and displacement history from this segment of the test procedure was to be modeled in the simulation run to support tuning of parameters governing structural damping and the SIM phenomenon. Plots of roller boundary displacement history and roller boundary force against displacement for a scenario characterized by a 167 mK s^{-1} temperature ramp and 1.00 N restraining force are illustrative of the test procedure (Figs. 5 and 6).

Although the length scale of the test article is orders of magnitude less than anticipated SMA deployed gossamer spacecraft systems, a model tuned at the dimensions of the specimen can be relevantly extended to any dimension, for a comparable amount of detwinned strain recovery at a comparable transformation rate, with a couple

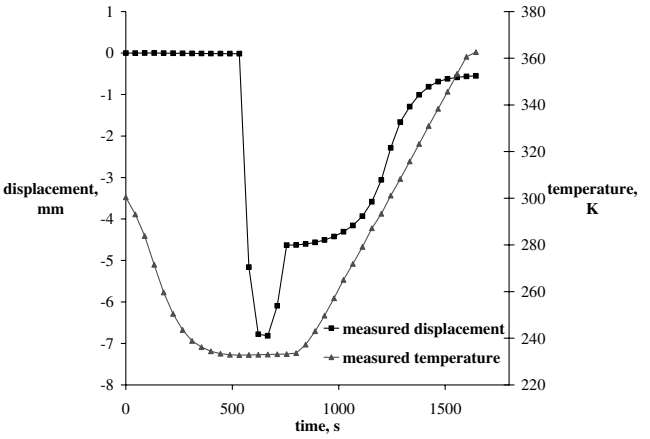

Fig. 5 Roller boundary displacement history experimental results of 167 mK s^{-1} temperature ramp and 1.00 N restraining force scenario.

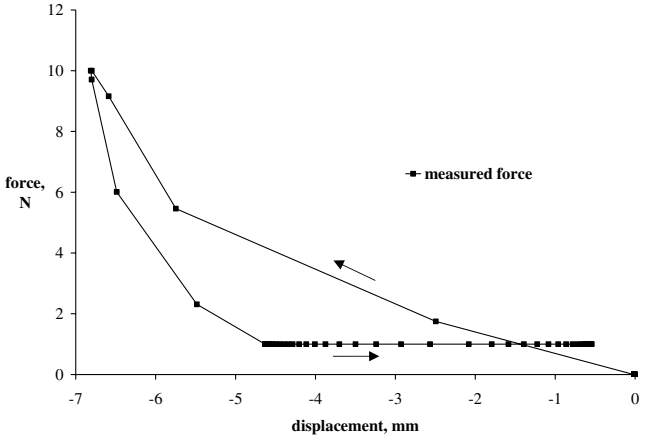

Fig. 6 Roller boundary force against displacement experimental results of 167 mK s^{-1} temperature ramp and 1.00 N restraining force scenario.

accuracy considerations since macroscopically the physics of the austenite nucleation are intensive phenomena and the subroutine interplays with the solid model through an intensive variable, strain. First, temperature measurement errors remain an intensive phenomenon. Uncertainty, within the bounds of the instrument's resolution, of the article's thermal state may error scaled predictions as to the sequencing of events, not their magnitude, that is, MTR may initiate over a temperature range within the instrument's resolution. Second, displacement measurement errors are extensive, but relate to measurement errors of the MTR rate, which is an intensive phenomenon. Aside from repeatability issues, which are not within the scope of this manuscript, uncertainty of the article's roller boundary position may error the pace of scaled predictions. Conservatively assuming the two displacement measurements reported in Fig. 5 capturing the specimen's greatest velocity response of 17.4 μm s^{-1} at approximately 1220 s were both erroneous at the extremes of the instrument's 1.00 nm resolution, the true velocity could vary by as much as 0.000259%, that is, the MTR rate of scaled SMA deployed systems could be as much as 0.000259% underpredicted and corresponding displacement, stress, and reaction force responses would be accordingly suspect.

2. *Model Refinement*

The MTR subroutine was customized to the fixed-roller boundary beam model to replicate the DMA experiments by varying expected influential, unknown parameters governing the SIM phenomenon and structural damping. The FEM was composed of 108 nodes. A three-dimensional model was considered to support development of the subroutine's utility for multidimensional behavior. The envisioned figure acquisition reproduced in Fig. 1 would involve radial spines and not a single axisymmetric actuator. The 108 nodes defined 26 ABAQUS C3D8RT elements as close to equal sided cubes as single element depth model representation would allow. Recognizably, the model was coarsely meshed to minimize computational expense. The B2 phase geometry is defined by Fig. 4. Material properties are consistent with those determined experimentally or published values [24,27].

At the onset it was apparent it would not be feasible to employ the ABAQUS Explicit solver for simulations of this duration due to the computational demanding integration method. The MTR subroutine was modified to interface with the ABAQUS Standard solver. Direct integration solutions are calculated at each time step to satisfy dynamic equilibrium. The kinematic state is advanced by employing the implicit Hilber–Hughes–Taylor operator developed from the trapezoidal rule, implemented iteratively with Newton's method for convergence of a nonlinear equation set [28]. Implications of this retooling to the thermal solution and timing aspects of the simulation run are discussed in [24].

These simulation runs were solved on a 32.0 bit, 5.60 GHz dual processor machine with 2.00 GB of RAM. Approximately 120 machine hours were required to complete a run. This investment could have been reduced approximately 60.0% by representing the test article with a two-dimensional model if three-dimensional performance was not of concern.

The scenario characterized by no restraining force was the first attempted to replicate. SIM behavior was discounted by valuing β at 1.57 rad. Rayleigh stiffness proportional damping was enforced at a nominal value of 10.0% of critical relative to the first austenitic mode.

To improve model fidelity, the Liang and Rogers phase transformation kinetics model was modified with an additional series of seven correction terms to capture the features of the SME distribution exhibited by the test article. Although the single term formulation of Eq. (1) may mimic the SME distribution of a single crystal SMA, this idealization cannot be expected of a polycrystalline SMA actuator in practice. These sinusoidal correction terms, with parameters found from a least squares fit to the experimental results to seek a more accurate simulation run solution, were typically cast in pairs to ensure continuity at the engagement and disengagement of the Liang and Rogers term [24]. The martensite phase fraction

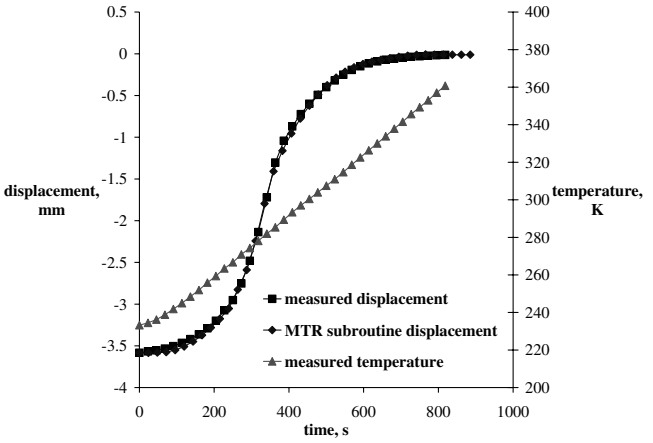

Fig. 7 MTR subroutine solution of roller boundary displacement history of 167 mK s^{-1} temperature ramp and no restraining force scenario with martensite phase fraction internal state variable correction terms.

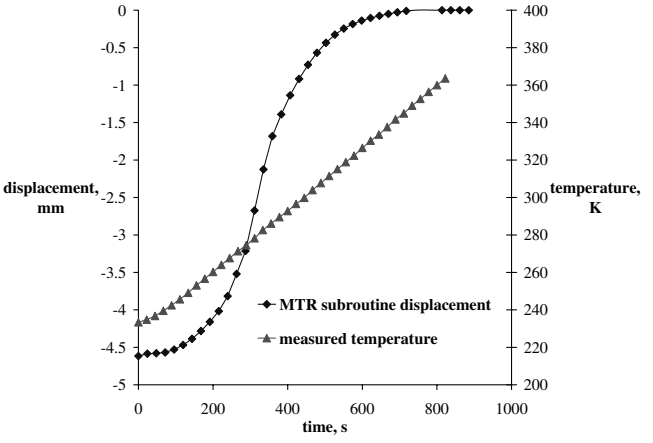

Fig. 8 MTR subroutine solution of roller boundary displacement history of 167 mK s^{-1} temperature ramp and 0.102 Kg mass scenario.

correction terms were incorporated into the MTR subroutine and the replication was again executed (Fig. 7).

As the stress state of the specimen was not significant, little could be gained from this scenario regarding the SIM parameter. With regard to structural damping, dependencies on this energy dissipation term were investigated more thoroughly considering the restraining force scenarios. The value in this scenario was the reformulation of the Liang and Rogers phase transformation kinetics model. With this refinement coded, efforts focused on replicating the restraining force experiments. (All subsequent simulation runs incorporated the seven martensite phase fraction correction terms in addition to the original Liang and Rogers phase transformation kinetics model into the MTR subroutine.)

The scenario characterized by a 1.00 N restraining force was the next attempted to replicate. SIM behavior was initially discounted by valuing β at 1.57 rad. Again, Rayleigh stiffness proportional damping was enforced at a nominal value of 10.0% of critical relative to the first austenitic mode. This simulation run encountered a numerical instability at approximately 100 s simulation time and faulted as the elements declarations were too distorted for convergence before any meaningful insight could be obtained.

Pollard [24] documents an investigation of the numerical artifacts which arise when modeling constant natural boundary conditions in attempt to map the SIM parameter window. Research performed by Bo et al. [29] proved insightful as to the experimentally measured value of this Nitinol material property. Extrapolating from the presented stress against temperature plots, the value of the SIM angle was interpreted as approximately 1.47 rad. To compare with the values coded in the MTR subroutine, this angle must be refigured for a nondimensional relationship. The nondimensional empirical value of the angle is approximately 1.41 rad with 358 K and 560 MPa as the values of the B2 phase finish temperature and the B2 phase yield stress, respectively. Pollard [24] also assesses the influence of structural damping; the MTR subroutine solutions were found to be insensitive to this parameter at the experimental phase transformation rates.

A zero gravity variant of the scenario characterized by a 1.00 N restraining force was executed. The constant boundary condition at the periphery was replaced with an equivalent mass of the 1.00 N weight force within a terrestrial gravitational field or 0.102 Kg. It was anticipated this inertial loading scenario would be representative of the deployment sequence predictions and consequently, it was necessary to determine any attributable instabilities or divergence trends. SIM behavior was accounted for by valuing β at 1.37 rad. Again, Rayleigh stiffness proportional damping was enforced at a nominal value of 10.0% of critical relative to the first austenitic mode (Fig. 8). (This simulation run yielded an intuitive roller boundary displacement history, with any numerical complications noticeably absent.)

III. Deployment Sequence

A. Deployment Model Design

The MTR subroutine was customized to represent an individual SMA radial actuator and corresponding concentrator sector of a spaceborne membrane optic SMA deployment actuator spine system to forecast the envisioned figure acquisition reproduced in Fig. 1 (Fig. 9). The imagined system architecture is composed of 36 circumferentially equally spaced SMA radial actuators. This model has the parent geometry of a parabolic profiled spine parallel to the x axis with the nominal dimensions of 1.00 m projected area radius, R_S, 10.0 mm square cross section thickness, h_S, and a focal length to diameter ratio $f_{\infty,S} = 0.500$ peripherally supporting a parabolic, polymeric reflector with the nominal dimensions of 1.00 m projected area radius, R_C, 25.0 μm thickness, h_C, 175 mm width, w_C, and a focal length to diameter ratio $f_{\infty,C}$ equal to unity. This shape is considered to be the equilibrium configuration of the aperture continuum reflecting current manufacturing concepts [30].

The cross section of the concentrator sector was considered prismatic along the radius or parallel to the x axis for this study and the curvature of the periphery boundary was approximated by the tangent to the polymeric reflector projected area at the spine interface. Rigid, beam, three-dimensional, and two-node (ABAQUS RB3D2) elements were modeled at this boundary appended to the SMA spine, effectively serving as the mechanical coupling between the two continuums; circumferential load paths were ignored by modeling the rigid elements along the tangent. These model reductions do not prohibit investigation of the transient thermal and radial stress states of the concentrator, expected to be of greatest concern.

The FEMs were composed of the legacy 108 nodes defining 26 ABAQUS C3D8RT elements format representing the spine and 162 nodes defining 130 shell, four-node, and reduced integration (ABAQUS S4R) elements representing the concentrator (Fig. 10). A three-dimensional model was considered as the deployment involves

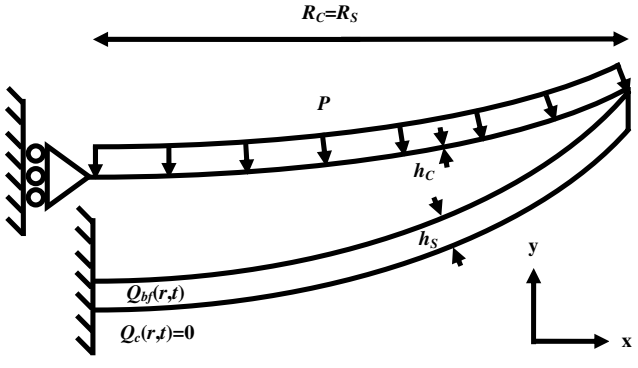

Fig. 9 Deployment spine and concentrator model.

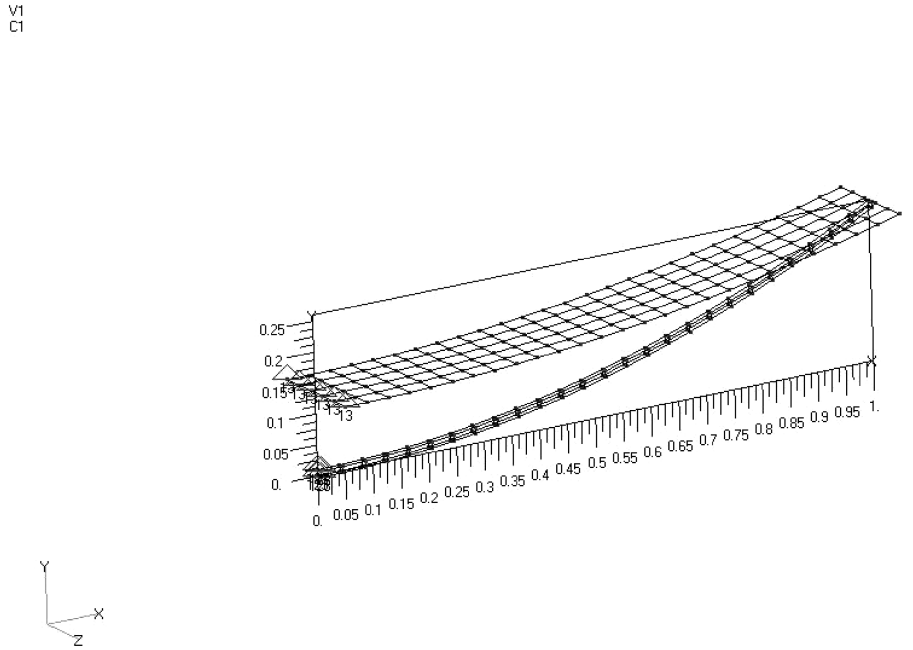

Fig. 10 FEM representation of the deployment spine and concentrator model with rigid elements at concentrator periphery boundary appended to the SMA spine.

multidimensional behavior. Envisioned figure acquisition reproduced in Fig. 1 would involve radial spines and not a single axisymmetric actuator. Recognizably, the model was coarsely meshed to minimize computational expenses.

Spine material properties, $E_S = 33.1$–57.0 GPa, $\upsilon_S = 0.330$, $\alpha_S = 6.62 \times 10^{-6}$–$1.20 \times 10^{-5}$ K^{-1}, $\rho_S = 6500$ kgm^{-3}, and $K_S = 8.60$–18.0 Wm^{-1} K^{-1}, are of SE-508, a representative Nitinol alloy. Concentrator material properties, $E_C = 2.80$ GPa, $\upsilon_C = 0.340$, $\alpha_C = 2.00 \times 10^{-5}$ K^{-1}, $\rho_C = 1420$ kgm^{-3}, $C_C =$ 1090 J kg^{-1} K^{-1}, and $K_C = 0.120$ Wm^{-1} K^{-1}, are of Kapton 100 HN®, representative of a polyimide material. Phase dependent properties independently sought include spine modulus of elasticity E_S and CTE α_S by employing DMA and thermomechanical analyzer (TMA) instruments, respectively. Thermal conductivity was assumed to be bounded with published values [27]. To accurately predict the thermomechanical response of any specimen of this alloy, it is requisite to determine these properties, as well as the B2 phase start and finish temperatures, from differential scanning calorimeter (DSC) testing of the specific material in hand [24].

To model thermal loads, effective specific heat as a function of temperature must be invoked for continuums undergoing phase changes. The term effective specific heat implies both the latent energy of the martensite to austenite phase transformation and the sensible heat rate are accounted for.

In addition to B2 start and finish temperatures, effective specific heat C_S was distilled from SE-508 DSC results. This material property as a function of temperature was found by numerically integrating the specific heat flow to gain a function of specific energy addition as a function of temperature. Numerically differentiating this intermediate solution by temperature results in the change in specific energy addition against temperature or effective specific heat. This relationship was fit to a second degree polynomial to be embedded in the MTR subroutine [Eq. (8)].

$$C_S(T) = -0.0288T^2 \frac{\text{J}}{\text{Kg K}^3} + 18.9T \frac{\text{J}}{\text{Kg K}^2} - 2340 \frac{\text{J}}{\text{Kg K}} \tag{8}$$

Natural and essential boundary conditions, $Q_{\text{bf}}(r,t)$, $Q_c(r,t)$, P, and plane symmetry of each model continuum, were enforced to simulate realistic deployment scenarios. Three specific thermal body flux load waveforms $q_{\text{bf}}(r,t)$ were considered within current projected on-orbit power budgets corresponding to three loading scenarios [Eqs. (9–11)] [31]. Thermal constraints restricted convective fluxes at all surfaces, that is, $Q_c(r,t) = 0$, and radiation effects were ignored.

$$q_{\text{bf}}(r,t) = 2.50 \times 10^6 \ \frac{\text{W}}{\text{m}^3} \qquad 0 \le t \le 188 \text{ s} \tag{9}$$

$$q_{\text{bf}}(r,t) = 1.25 \times 10^6 \ \frac{\text{W}}{\text{m}^3} \qquad 0 \le t \le 376 \text{ s} \tag{10}$$

$$q_{\text{bf}}(r,t) = 5.32 \times 10^4 \ \frac{\text{W}}{\text{m}^3\text{s}} t \qquad 0 \le t < 94.0 \text{ s} \tag{11}$$

$$q_{\text{bf}}(r,t) = 5.00 \times 10^6 \ \frac{\text{W}}{\text{m}^3} - 5.32 \times 10^4 \ \frac{\text{W}}{\text{m}^3\text{s}} (t - 94.0 \text{ s})$$
$$94.0 \le t < 188 \text{ s}$$

$$q_{\text{bf}}(r,t) = 0 \qquad t > 188 \text{ s}$$

Consistent with general control methodology of membrane optics, all scenarios included a uniform, bias, 1.00 Pa, surface-normal, and constant load acting on the concentrator. This load could be provided by gas or, to avoid attendant makeup gas and lenticular complications, electrostatic pressure. It is expected some degree of self-rigidization will be required to not only acquire the deterministic figure, but also for maintenance of the polymeric reflector's figure, even with the aid of a strain coating [30]. The aperture was mechanically constrained from translations in the directions of the x- and z-unit vectors, with translations in the direction of the y-unit vector and rotational DOFs unconstrained, at the vertex boundary and the spine was mechanically constrained from all three translations at the vertex boundary, consistent with the quasi-axisymmetric reduction of the model.

The R phase geometry of the SMA spine and deformed state of the polymeric reflector were found by elastically translating the two interface nodes at the periphery (1.000 m, 0.260 m), of the model in the direction of the negative x-unit vector to the vertical axis (0.000 m, 0.811 m), while not permitting translations of these nodes

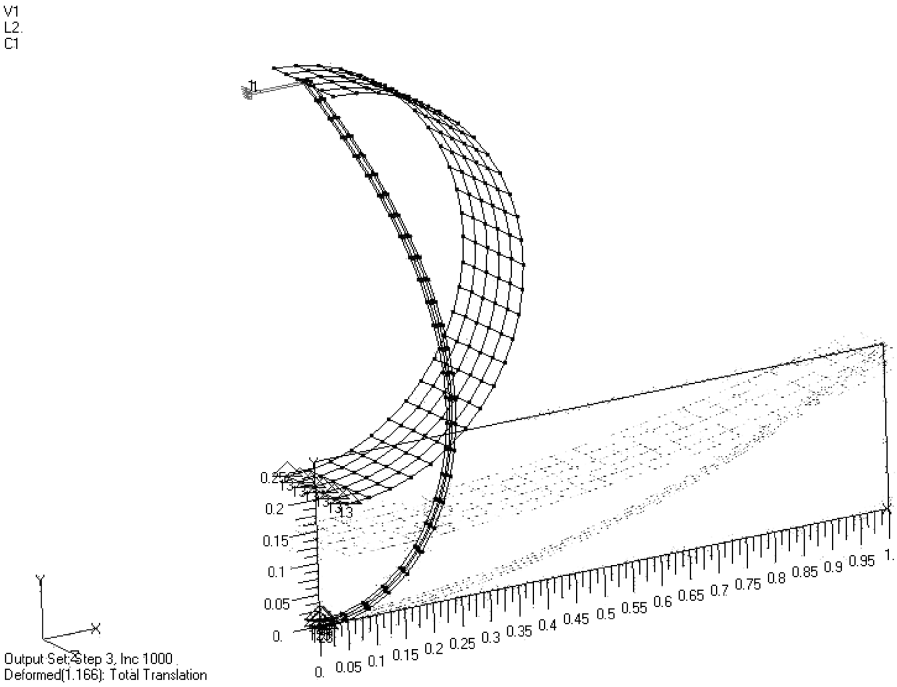

Fig. 11 R phase geometry of the SMA spine and deformed state of the polymeric reflector.

parallel to the z axis (Fig. 11). Shell, four-node, and full integration (ABAQUS S4) elements were used and contact phenomenon was discounted. The ABAQUS static solver was employed. This finite element analysis maintained the essential boundaries at the respective vertices of each continuum and the natural boundary condition prescribed at the surface of the concentrator, with nonlinear deformation invoked. This global geometry is characterized by a maximum principal spine strain of 8.43% occurring in element 26 at the periphery and qualifying within the maximum recoverable strain limit for one time actuation of Nitinol [6]. Considered as the stowed configuration, this packaging reduces the projected area radius of the observatory by approximately one-third.

Based on the computational capacity limitations encountered with refinement efforts, which precluded the feasibility of employing the ABAQUS Explicit solver for simulations of the duration of the experimental scenarios due to the computational demanding integration method, it was anticipated the ABAQUS Standard solver would be used for the deployment sequence predictions as well. Implications of this retooling to the thermal solution and timing aspects of the simulation run are discussed, and an additional complexity associated with this simulation run as the model comprises components which do not undergo a change in static equilibrium state, that is, the concentrator, is addressed in [24].

SIM behavior was accounted for by valuing β at 1.37 rad. Rayleigh stiffness proportional or viscous material damping was enforced at 10.0% of critical relative to the first modes of both the austenitic spine and concentrator. Enforcing energy dissipation through this linear construct accounts for internal friction of the original crystallographic structure recovery of the spine and possible radiative damping, a manifest of the bias pressure load on the concentrator. Pollard [24] details further development of the MTR subroutine relevant to forecasting the deployment sequence.

B. Deployment Model Results

The scope of this study was to model the relation of input power magnitude and waveform to stress fields, reaction forces, and thermal fields for the figure acquisition of a gossamer, polymeric reflector. Of particular interest is the stress and thermal field history of the polymeric membrane concentrator through the deployment to prevent mechanical and thermal failure as limited experimental or modeling analysis results exist for SMA deployment schemes.

The MTR subroutine simulation run solution enforcing the step waveform body flux loading scenario defined by Eq. (9) yielded an intuitive global response. Stills of the SMA spine's detwinned strain recovery are illustrated at 57.6 and 115 s simulation run time (Fig. 12).

The figure acquisition simulation run solutions enforcing a step waveform body flux loading scenario periphery displacement histories present a more detailed perspective of the deployment (Fig. 13). Temperature history of the interface is also plotted.

The vibration behavior present in all three y-displacement histories preceding the deployed equilibrium excursions range from 0.077 to 0.160 Hz for a four cycle average of the responses excited by the load waveform scenarios defined by Eqs. (10) and (11),

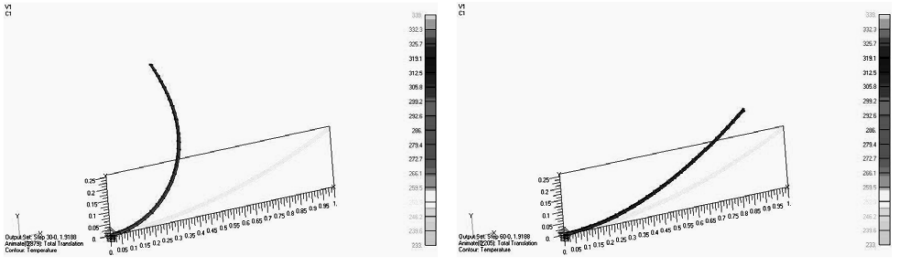

a) b)

Fig. 12 Spine FEM detwinning strain recovery responding to Eq. (9) step waveform body flux loading scenario, a) at 57.6 s simulation run time; b) at 115 s simulation run time.

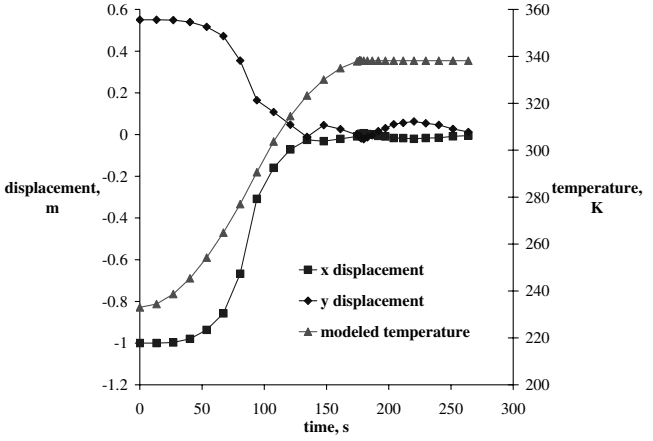

Fig. 13 MTR subroutine solution of periphery *x* and *y* displacement and temperature history responding to Eq. (9) step waveform body flux loading scenario.

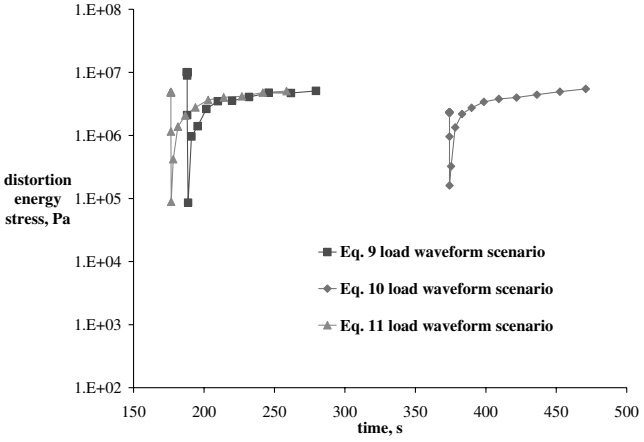

Fig. 15 MTR subroutine full solution of concentrator periphery distortion energy stress history responding to Eqs. (9–11) waveform body flux loading scenarios.

respectively. The frequency of the first austenitic mode of the spine in the unloaded equilibrium configuration, divorced from the concentrator, was found to occur at 0.521 Hz. One would expect the natural frequency of the spine and concentrator integrated model in an intermediate phase state to be less than this property, with the mass of the concentrator effecting at the periphery and devalued elastic modulus. The period of the first excursion cycle following aperture tensioning for all three scenarios was approximately 90.0–95.0 s, most probably the natural period of the integrated model excited by the concentrator engagement.

Distortion energy stress history is reported at the periphery of the spine from the three simulation run solutions (Fig. 14). These contours are the running sum of the elastic and inelastic stress terms of the unified constitutive relation introduced as Eq. (2).

Distortion energy stress history is also reported at the periphery of the concentrator from the three simulation run solutions (Fig. 15). [The simulation run solution enforcing the step waveform body flux loading scenario defined by Eq. (10) achieved a stress state relatively higher than initial tensioning, with respect to the other two scenarios, as the velocity for this loading regime was opposite sense upon concentrator engagement, returning from an excursion.] Reasoning for the conservatism of the reflector stress histories due to model reductions is supported in [24].

Reaction forces are reported as the sum of the *y* components at the four spine vertex nodes (Fig. 16). Nodes of continuum elements do not have rotational DOFs; reaction moments were not found. (One would expect the symmetric *x*-component forces to be countered by the opposing spine and concentrator sector pairs and the asymmetric and net *y*-component forces to be communicated to the vehicle bus.) Reaction forces at the model transition are truncated. Maximum *x*- and *y*-reaction forces for the three loading scenarios were approximately 2500 and 300 N, respectively.

Temperature history of the reflector periphery can be plotted throughout the entire simulation run (Fig. 17). Thermal authority over the concentrator was found locally limited to the periphery; the polyimide conductivity is from 1 and 2 orders of magnitude less than the conductivity of the SMA between R and B2 crystalline phases.

Additional R phase configurations should be considered to support optimal packaging strategies and exact B2 phase geometries should be determined, dictated by concentrator position and reaction force demands. Conceptual, collapsible architectures for membrane reflectors of merit have been proposed [32,33]. The seminal work of Mikulas [34] and Hedgepeth [35] reasoned large space vehicles are more susceptible to on-orbit loads and these factors drive the basic parameters for deployed designs.

In addition to the required quasi-static boundaries afforded by the spines, concentrator demands include stiffness to reduce the wave front error to be actively managed resulting from time varying disturbances. Dynamic stability scaling laws based on structural modal frequency and damping ratio relating aperture dimensions to structural depth and material specific modulus have been presented by Peterson and Hinkle [36]. Structural deformation sensitivity was found to scale inversely with the square of structural depth and inversely with the material specific modulus.

Parallel research complimentary to the spine and concentrator model has been performed concerning the management of in-service aberration phenomenon. The scope of this study consists of characterizing the nonlinear dynamic behavior of membrane

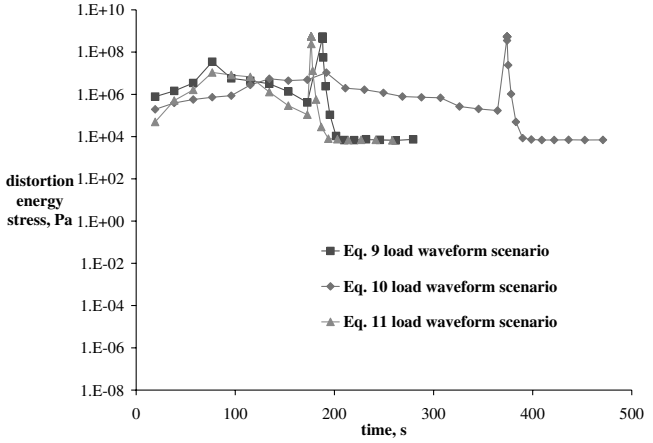

Fig. 14 MTR subroutine solution of spine periphery distortion energy stress history responding to Eqs. (9–11) waveform body flux loading scenarios.

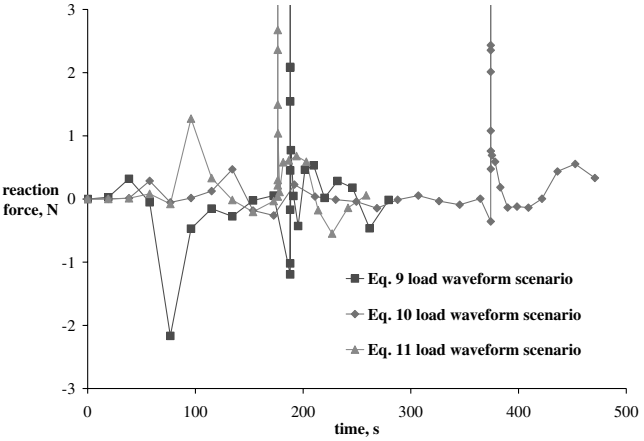

Fig. 16 MTR subroutine full solution of spine vertex *y*-reaction force history responding to Eqs. (9–11) waveform body flux loading scenarios.

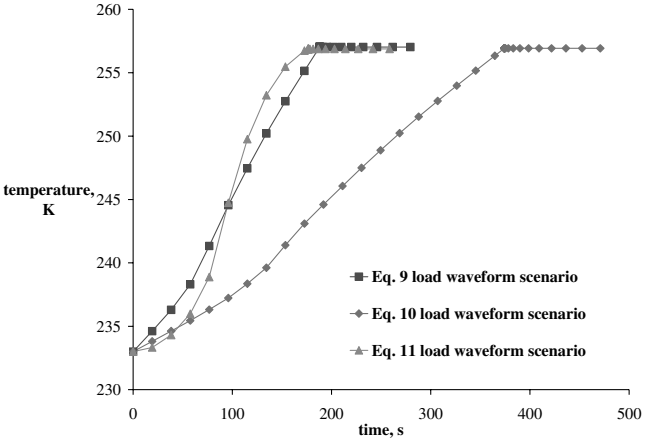

Fig. 17 MTR subroutine full solution of concentrator periphery temperature history responding to Eqs. (9–11) waveform body flux loading scenarios.

reflectors to visible optics quality under realistic support and loading scenarios. The objective of this work was to investigate the nonlinear characteristics of the dynamic behavior of membrane optics as the basis for future work in system identification and figure control [37]. Further considerations of model error limits, constitutive relation derivations, and numerical implementation have been combined by deBlonk [38] into a guideline for modeling the optical level structural behavior of curved membrane mirrors.

IV. Discussions and Conclusions

A. Deployment Sequence

The deployment sequence modeling efforts were insightful for both forecasting the figure acquisition of a gossamer, polymeric reflector harnessing the SME and the performance capabilities of the MTR subroutine. The three waveform body flux loading scenarios activated rhombohedral to B2 phase transformations of the SMA spine within approximately 177–374 s. Upon reflector engagement, the integrated model's first excursion cycle frequency excited by all three loading regimes was nonunique, regardless of the temporal character preceding the aperture tensioning. This tendency suggests a coupling between the structural dynamic designs for deployment and in-service, deployed architectures. Distortion energy stress and temperature histories documented through these simulation runs are indicative of the mechanical and thermal demands on the two continuums. Features of these load trends are relevant to other SMA actuation schemes.

Distortion energy stress magnitudes at the periphery regions of the spine followed the phase transformation kinetics; greater stresses were reported midway through the B2 crystalline structure recovery corresponding to the more rapid transformation rates at these unstable minima and consequently greater inertial loads communicated through the SMA continuum. The mechanical loads were significant upon engaging the aperture. (These stress spikes are within Nitinol's austenite proportional limit range.) These two load trends are reflected in the reaction force histories of the simulation run solutions.

The distortion energy stress magnitudes at the periphery region of the reflector reported upon initial tensioning should be regarded as the extreme for aperture engagement. Initial tensioning of the polymeric reflector is pronounced at each projected area radius of all three loading scenarios. The subsequent increase in distortion energy stress manifests upon retensioning due to a subsequent excursion cycle. (Only the initial tensioning stress at the periphery of the figure acquisition simulation run solution enforcing the full-power step waveform body flux loading scenario exceeded the proportional limit of Kapton 100 HN®.)

These mechanical load trends decreased from the full-power step to the step waveform body flux loading scenario at half-power and to the symmetrical linear waveform body flux loading scenario, effectively motivating the phase transformation at a pace tantamount to the full-power step. All three body flux loading scenarios imparted an equitable amount of energy to the system and consequently the final temperature realized in the aperture near the interface was not unique.

Aspects of the deployment sequence warranting further study include determining the effects of radiation load paths on the character of the response and investigating an unreduced model to perceive true three-dimensional phenomena including circumferential stress states and asymmetric loading of the reflector. To facilitate figure maintenance, detailed models could incorporate interfaces between the spine and aperture at multiple projected area radii and account for imaging and electrostatic hardware affixed to the spine.

B. MTR Subroutine

The development and refinement of an SMA modeling approach, the MTR subroutine, has been presented. In concert with the commercial finite element solver, ABAQUS Explicit, this application supports multidimensional, temperature-displacement transient predictions of the SME exhibited by SMAs through implementation of a phenomenological constitutive law. This article presents an original notion to numerically describe a multiaxial, inelastic response of a continuum with a standard of practical utility not previously considered in the literature. The subroutine capability is limited to one-way phase transformation, from martensite to austenite, attendant detwinned strain recovery; two-way, superelasticity, and conventional plastic deformation behavior is not supported.

The greatest asset of model refinement is the confidence established knowing documented numerical instabilities and divergence trends of the MTR subroutine modeling approach are not associated with simulation runs involving inertial loads. This credence staged the forecasting of the transient response of a spaceborne membrane optic SMA deployment actuator spine system, the headlining objective of this thesis research, and also establishes confidence in the amenability of the approach to schemes implementing the SME to reconfigure and tune monolithic structures or actuate mechanical systems not involving constant natural boundary conditions.

Aspects of the MTR subroutine warranting further study include tracking and quantifying the systemic influences of the boundary condition steps' energy contributions and timing of the simulation run step. The effect order on the simulation run solution of assuming the SIM angle as a constant value through the phase transformation is worth consideration to perhaps enable greater fidelity. Three pertinent issues arose from the deployment sequence. Scalability of the parameter window mapped for one-way behavior from replicating experiments, with SMA test articles undergoing significantly less detwinned strain recovery, deserves some scrutiny. It is evident from stills of the spine finite element models the inclusion of logic, implementing compatibility theory to ensure conservation of mass of shape changing continuums, is required for greater fidelity of SME predictions with relatively large attendant translations and rotations. Continued development of the MTR subroutine to support two-way SME behavior is a manifold issue for tackle. Revising the approach to support this phenomenon would render the subroutine capable of throughput packaging and deployment design. One could envision a reversal of the constituent hypothesis to permit and account detwinning strain accumulation at the threshold stress and until the maximum recoverable strain limit.

Just as space vehicles first incorporated the SME, deployment and in-service challenges of gossamer spacecraft, such as the transient response of a spaceborne membrane optic SMA deployment actuator spine system addressed through this thesis research, will further showcase the leverage SMA technology extends to structural reconfiguration and tuning to foster and mature successive large, launch-packaged space vehicle programs.

Acknowledgment

Support of this research is provided by an award from the Air Force Research Laboratory Space Vehicles Directorate coordinated by Jeffry S. Welsh.

References

[1] Birman, V., "Review of Mechanics of Shape Memory Alloy Structures," *Applied Mechanics Reviews*, Vol. 50, No. 11, 1997, pp. 629–645.

[2] Lucy, M., Hardy, R., Kist, E., Watson, J., and Wise, S., "Report on Alternative Devices to Pyrotechnics on Spacecraft," NASA TM-110470, 1996.

[3] *Gossamer Spacecraft: Membrane and Inflatable Structures Technology for Space Applications*, edited by C. H. M. Jenkins, Progress in Astronautics and Aeronautics, AIAA, Washington, D.C., 2001.

[4] Chang, L. C., and Read, T. A., "Plastic Deformation and Diffusionless Phase Changes in Metals—The Gold-Cadmium Beta Phase," *Journal of Metals*, Vol. 191, No. 1, 1951, pp. 47–52.

[5] Buehler, W. J., Gilfrich, J. V., and Wiley, R. C., "Effect of Low-Temperature Phase Changes on the Mechanical Properties of Alloys Near Composition TiNi," *Journal of Applied Physics*, Vol. 34, No. 5, 1963, pp. 1475–1477.

[6] Cross, W. B., Kariotis, A. H., and Stimler, F. J., "Nitinol Characterization Study," NASA CR-1433, 1970.

[7] Proft, J. L., and Duerig, T. W., "Mechanical Aspects of Constrained Recovery," *Engineering Aspects of Shape Memory Alloys*, edited by T. W. Duerig, K. N. Melton, D. Stockel, and C. M. Wayman, Butterworth–Heinemann, London, U.K., 1990, pp. 115–129.

[8] Tanaka, K., and Nagaki, S., "A Thermomechanical Description of Materials with Internal Variables in the Process of Phase Transitions," *Ingenieur Archive*, Vol. 51, No. 5, 1982, pp. 287–299.

[9] Liang, C., and Rogers, C. A., "One-Dimensional Thermomechanical Constitutive Relations for Shape Memory Materials," *Journal of Intelligent Material Systems and Structures*, Vol. 1, No. 2, 1990, pp. 207–234.

[10] Ivshin, Y., and Pence, T. J., "A Constitutive Model for Hysteretic Phase Transition Behavior," *International Journal of Engineering Science*, Vol. 32, No. 4, 1994, pp. 681–704.

[11] Brinson, L. C., "Constitutive Behavior of Shape Memory Alloys: One-Dimensional Thermomechanical Derivation with Non-Constant Material Functions and Redefined Martensite Internal Variable," *Journal of Intelligent Materials Systems and Structures*, Vol. 4, No. 2, 1993, pp. 229–242.

[12] Boyd, J. G., and Lagoudas, D. A., "Thermomechanical Response of Shape Memory Composites," *Proceedings of SPIE's 1993 Smart Structures and Materials Conference*, edited by N. W. Hagood and G. J. Knowles, Vol. 1917, SPIE, Bellingham, WA, 1993, pp. 774–790.

[13] Abeyaratne, R., Kim, S. J., and Knowles, J. K., "One-Dimensional Continuum Model for Shape Memory Alloys," *International Journal of Solids and Structures*, Vol. 31, No. 16, 1994, pp. 2229–2250.

[14] Brinson, L. C., and Huang, M. S., "Simplifications and Comparisons of Shape Memory Alloy Constitutive Models," *Journal of Intelligent Materials Systems and Structures*, Vol. 7, No. 1, 1996, pp. 108–118.

[15] Sun, Q. P., and Hwang, K. C., "Micromechanics Modeling for the Constitutive Behavior of Polycrystalline Shape Memory Alloys-1,2," *Journal of the Mechanics and Physics of Solids*, Vol. 41, No. 1, 1993, pp. 1–33.

[16] Patoor, E., Eberhardt, A., and Berveiller, M., "Micromechanical Modeling of the Shape Memory Behavior," *Mechanics of Phase Transformation and Shape Memory Alloys*, edited by L. C. Brinson and B. Moran, ASME, New York, 1994, pp. 23–37.

[17] Goo, B. C., and Lexcellent, C., "Micromechanics-Based Modeling of Two-Way Memory Effect of a Single Crystalline Shape-Memory Alloy," *Acta Metallurgica el Materialia*, Vol. 45, No. 2, 1997, pp. 727–737.

[18] Huang, M. S., and Brinson, L. C., "A Multivariant Model of Single Crystal Shape Memory Alloys," *Journal of the Mechanics and Physics of Solids*, Vol. 46, No. 8, 1998, pp. 1379–1409.

[19] Vivet, A., and Lexcellent, C., "Micromechanical Modeling for Tension-Compression Pseudoelastic Behavior of AuCd Single Crystals," *European Physical Journal, Applied Physics*, Vol. 4, No. 2, 1998, pp. 125–132.

[20] Lu, Z. K., and Weng, G. J., "Martensitic Transformations and Stress-Strain Relations of Shape-Memory Alloys," *Journal of the Mechanics and Physics of Solids*, Vol. 45, Nos. 11–12, 1997, pp. 1905–1928.

[21] Vokoun, D., and Kafka, V., "Mesomechanical Modelling of Shape Memory Effect," *Proceedings of SPIE's 6th Annual International Synopsis on Smart Structures and Materials*, edited by V. V. Varadan, Vol. 3667, SPIE, Bellingham, WA, 1999, pp. 596–601.

[22] Liang, C., and Rogers, C. A., "Multi-Dimensional Constitutive Relations of Shape Memory Alloys," *Proceedings of the 32nd AIAA/ASME/ASCE/AHS/ASC Structures, Structural Dynamics, and Materials Conference*, AIAA, Washington, D.C., 1991; also AIAA Paper 1991-1165.

[23] Brocca, M., Brinson, L. C., and Bazant, Z. P., "Three Dimensional Constitutive Model for Shape Memory Alloys Based on Microplane Model," *Journal of the Mechanics and Physics of Solids*, Vol. 50, No. 5, 2002, pp. 1051–1077.

[24] Pollard, E. L., "Shape Memory Alloy Deployment of Membrane Mirrors for Spaceborne Telescopes," Master's Thesis, Mechanical Engineering Dept., South Dakota School of Mines & Technology, Rapid City, SD, 2004.

[25] ABAQUS/Explicit User's Manual, Hibbitt, Karlsson, & Sorensen, Inc., 2004.

[26] TA Instruments Dynamic Mechanical Analyzers, TA Instruments, 2004.

[27] Hodgson, D. E., Wu, M. H., and Biermann, R. J., "Shape Memory Alloys," Johnson Matthey, 2004.

[28] ABAQUS/Standard User's Manual, Hibbitt, Karlsson, & Sorensen, Inc., 2004.

[29] Bo, Z., Lagoudas, D. C., and Miller, D., "Material Characterization of SMA Actuators Under Non-Proportional Thermomechanical Loading," *Journal of Engineering Materials and Technology*, Vol. 121, No. 1, 1999, pp. 75–85.

[30] Ash, J. T., Jenkins, C. H., Marker, D. K., and Wilkes, J. M., "Shape Achievement of Optical Membrane Mirrors Using Coating/Substrate Intrinsic Stresses," *Journal of Spacecraft and Rockets*, Vol. 41, No. 4, 2004, pp. 551–557.

[31] Jilla, C. D., and Miller, D. W., "Satellite Design: Past, Present, and Future," *International Journal of Small Satellite Engineering*, Vol. 1, No. 1, 1995.

[32] Lai, C. Y., and Pellegrino, S., "Deployable Membrane Reflectors with Offset Configurations," *Proceedings of the 40th AIAA/ASME/ASCE/AHS/ASC Structures, Structural Dynamics, and Materials Conference*, AIAA, Washington, D.C., 1999; also AIAA Paper 1999-1477.

[33] Baier, H., Datashvili, L., Gogava, Z., Medzmariashvili, E., and Montuori, V., "Building Blocks of Large Deployable Precision Membrane Reflectors," *Proceedings of the 42nd AIAA/ASME/ASCE/AHS/ASC Structures, Structural Dynamics, and Materials Conference*, AIAA, Washington, D.C., 2001; also AIAA Paper 2001-1478.

[34] Mikulas, M. M., "Structural Efficiency of Long and Lightly Loaded Truss and Isogrid Columns for Space Applications," NASA TM-78687, 1978.

[35] Hedgepeth, J. M., "Critical Requirements for the Design of Large Space Structures," NASA CR-3484, 1981.

[36] Peterson, L. D., and Hinkle, J. D., "Implications of Structural Design Requirements for Selection of Future Space Telescope Architectures," *Proceedings of SPIE's 2003 Conference on Optical Science & Technology*, edited by H. A. MacEwen, Vol. 5166-05, SPIE, Bellingham, WA, 2003.

[37] Pollard, E. L., deBlonk, B. J., Erwin, R. S., and Jenkins, C. H. M., "Characterizing the Non-Linear Dynamic Behavior of Membrane Optics," *Proceedings of SPIE's 2004 Conference on Optical Science & Technology*, edited by L. D. Peterson and R. C. Guyer, Vol. 5528A-22, SPIE, Bellingham, WA, 2004.

[38] deBlonk, B. J., "Optical-Level Structural Modeling of Membrane Mirrors for Spaceborne Telescopes," Ph.D. Thesis, Aeronautics and Astronautics Dept., Massachusetts Institute of Technology, Cambridge, MA, 2003.

G. Agnes
Associate Editor